Available on the CERN CDS information server **CMS PAS SUS-16-044**

CMS Physics Analysis Summary

Contact: cms-pag-conveners-susy@cern.ch 2017/03/22

Search for the pair production of Higgsinos in pp collisions at $\sqrt{s} = 13$ TeV in final states with Higgs bosons and large missing transverse momentum

The CMS Collaboration

Abstract

Results are reported from a search for new physics in proton-proton collisions leading to an experimental signature with two Higgs bosons and large missing momentum in the direction transverse to the beam axis. This signature can arise in the context of supersymmetry, where a broad class of models predicts the electroweak production of a pair of Higgsinos, each of which can decay via a cascade process to a final state with a Higgs boson and the lightest supersymmetric particle (LSP). The LSPs remain undetected, producing the large missing transverse momentum characteristic for these events. The search uses a 35.9 fb^{-1} sample of proton-proton collision data at $\sqrt{s} = 13$ TeV, accumulated by the CMS experiment at the LHC. The observed event yield in the signal region is found to be consistent with the expected standard model background predicted from control regions in the data. Higgsinos with mass in the range $225 - 770$ GeV are excluded at 95% CL using a simplified model framework for the production and decay of approximately degenerate Higgsinos in the context of gauge mediated supersymmetry breaking.

1 Introduction

The discovery of a Higgs boson with a mass $m_{\mathrm{h}} \approx 125$ GeV [1–6] at the electroweak scale provides a new tool that can be used in searches for particles associated with physics beyond the standard model (SM). Particles predicted by models based on supersymmetry (SUSY) [7–14] are expected in many cases to decay into Higgs bosons with significant branching fractions, and in some cases, the presence of a Higgs boson can become a critical part of the experimental signature [15–17].

In this analysis, we perform a search for processes leading to Higgs-boson pair production in association with large magnitude of the missing transverse momentum vector, $\vec{p}_{\mathrm{T}}^{\mathrm{miss}}$, with each Higgs particle decaying via its dominant decay mode, $\mathrm{h} \to \mathrm{b\bar{b}}$, which has a branching fraction of around 60%. Such a signature can arise, for example, in models based on SUSY, in which an electroweak process can lead to the production of two supersymmetric particles, each of which decays into a Higgs boson and another particle that interacts so weakly that it escapes detection in the apparatus. The search uses an event sample of proton-proton collision data at $\sqrt{s} = 13$ TeV, corresponding to an integrated luminosity of 35.9 fb^{-1}, accumulated by the CMS experiment at the CERN LHC. Searches for this and related decay scenarios have been performed by ATLAS [18, 19] and CMS [15, 17, 20] using 7 TeV and 8 TeV data. In particular, this analysis is based on an approach developed in Ref. [15].

While the Higgs particle completes the SM, the low value of its mass raises fundamental questions that suggest the existence of new physics beyond the SM. Assuming that the Higgs boson is a fundamental (that is, non-composite) spin-0 particle, stabilizing its mass at the electroweak scale is a major theoretical challenge, referred to as the gauge hierarchy problem [21–26]. Specifically, without invoking new physics, preventing the Higgs boson mass from being pulled by quantum loop corrections to the cutoff scale of the theory, which can be taken as, for example, the Planck scale, requires extreme degree of fine tuning of the theoretical parameters. Instead, this stabilization can be achieved through a variety of mechanisms extending the SM, such as supersymmetry (SUSY) or extra dimensions.

A class of so-called natural SUSY models [27–30] contain the ingredients necessary to stabilize the Higgs boson mass at the electroweak scale, and are thus the object of intensive searches at the LHC. In any SUSY model, additional particles are introduced such that all fermionic (bosonic) degrees of freedom in the SM are paired with corresponding bosonic (fermionic) degrees of feedom in the extended theory. In natural SUSY models, certain classes of partner particles are expected to be light. These include the four Higgsinos ($\tilde{\mathrm{H}}^0_{1,2}$, $\tilde{\mathrm{H}}^{\pm}$), both top squarks, $\widetilde{\mathrm{t}}_L$ and $\widetilde{\mathrm{t}}_R$, which have the same electroweak couplings as the left- (L) and right- (R) handed top quarks, respectively; the bottom squark with L-handed couplings ($\widetilde{\mathrm{b}}_L$); and the gluino ($\widetilde{\mathrm{g}}$). Of these, the Higgsinos are generically expected to be the lightest, but in contrast to the squarks and the gluino which couple via the strong force, the Higgsinos only couple via electroweak interactions, greatly suppressing their production cross sections. Furthermore, in natural scenarios, the four Higgsinos are approximately degenerate in mass, so that transitions among these SUSY partners would typically produce only very soft additional particles, which do not contribute to the experimental signature.

More generally, the gaugino and Higgsino fields can mix, leading to mass eigenstates that are classified either as neutralinos ($\tilde{\chi}^0_i, i = 1-4$) or charginos ($\tilde{\chi}^{\pm}_i, i = 1-2$.) If the $\tilde{\chi}^0_1$ is the lightest supersymmetric particle (LSP), it is stable in R-parity [31] conserving models and, because of its weak interactions, would escape experimental detection. Searches for the direct production of such particles can be performed using signatures involving initial-state radiation, in which

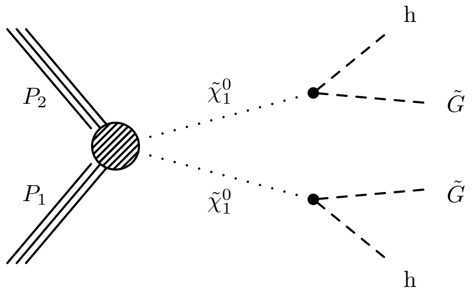

Figure 1: Diagram for the gauge-mediated-symmetry-breaking signal model, $\tilde{\chi}_1^0\tilde{\chi}_1^0 \to \mathrm{hh}\tilde{G}\tilde{G}$ (TChiHH), where $\tilde{G}$ is a Goldstino. The NLSPs χ_1^0 are not directly pair produced, but are instead produced in the cascade decays of several different combinations of neutralinos and charginos, as described in the text.

a hadronic jet or energetic photon is radiated before the hard-scattering of the partons. The jet or photon then recoils against the missing transverse momentum. Such monojet searches have been performed by both ATLAS [32] and CMS [33], but, thus far, no signals have been observed.

While crucial to addressing the question of naturalness, the detection of particles in a nearly degenerate Higgsino sector that contains the LSP poses a major experimental challenge. However, there is an alternative scenario in which the lightest Higgsino/neutralino is not the lightest supersymmetric particle, but the next- to-lightest supersymmetric particle (NLSP). The LSP can be another particle that is generic in SUSY models, the Goldstino ($\tilde{\mathrm{G}}$). The Goldstino is the Nambu-Goldstone particle associated with the spontaneous breaking of global supersymmetry and is a fermion. In a broad range of models in which SUSY breaking is mediated at a low scale, such as Gauge Mediated Supersymmetry Breaking (GMSB) models [34, 35], the Goldstino is nearly massless on the scale of the other particles and becomes the LSP. If SUSY is promoted to a local symmetry, leading to gravity, the Goldstino is “eaten” by the SUSY partner of the graviton, the gravitino ($J = 3/2$), and provides two of its four degrees of freedom. In the region of parameter space involving prompt decays to the gravitino, only the degrees of freedom associated with the Goldstino have sufficiently large couplings to be relevant, so it is common to denote the particle in either case as a Goldstino. In these GMSB models, the Goldstino mass is generically at the eV scale.

If the lighter neutralinos and charginos are dominated by their Higgsino content and are thus nearly mass degenerate, their cascade decays can all lead to the lightest neutralino, $\tilde{\chi}_1^0$ (now taken to be the NLSP), plus soft particles. Integrating over the contributions from various allowed combinations of produced charginos and neutralinos ($\tilde{\chi}_1^0\tilde{\chi}_2^0$, $\tilde{\chi}_1^0\tilde{\chi}_1^\pm$, $\tilde{\chi}_2^0\tilde{\chi}_1^\pm$, $\tilde{\chi}_1^\pm\tilde{\chi}_1^\mp$) therefore leads to an effective rate for $\tilde{\chi}_1^0\tilde{\chi}_1^0$ production [36, 37] that is significantly larger than that for any of the individual primary pairs resulting in a boost to the experimental sensitivity. The Higgsino-like NLSP would then decay via $\tilde{\chi}_1^0 \to (\gamma, \mathrm{h}, \mathrm{Z})\tilde{\mathrm{G}}$, where the Goldstino can lead to large $\vec{p}_{\mathrm{T}}^{\mathrm{miss}}$. The branching fractions here depend on a number of parameters including $\tan\beta$, the ratio of the Higgs vacuum expectation values, but the branching fraction for $\tilde{\chi}_1^0 \to \mathrm{h}\tilde{\mathrm{G}}$ can be substantial. As a consequence, the signature hh + $\vec{p}_{\mathrm{T}}^{\mathrm{miss}}$ with $\mathrm{h} \to \mathrm{b\bar{b}}$ can provide sensitivity to the existence of a Higgsino sector in the important class of scenarios in which the LSP mass lies below the Higgsino masses.

Figure 1 shows the pair production of two $\tilde{\chi}_1^0$ NLSPs, each decaying via $\tilde{\chi}_1^0 \to \mathrm{h}\tilde{\mathrm{G}}$, where it is assumed that the NLSPs are each fed by the production of $\tilde{\chi}_1^0$, $\tilde{\chi}_2^0$, and $\tilde{\chi}_1^\pm$ as described above. This situation arises when the mass splittings among charginos and neutralinos are large enough ($\gtrsim$ 100 MeV) so that the decays to $\tilde{\chi}_1^0$ occur promptly, while also small enough so that the additional soft particles fall out of acceptance. This scenario, in which other potential NLSP decay modes are ignored, is a SUSY simplified model [38–40] and is designated by TChiHH.

2 Detector

The central feature of the CMS detector is a superconducting solenoid of 6 m internal diameter, providing a magnetic field of 3.8 T. Within the solenoid volume are the tracking and calorimeter systems. The tracking system, composed of silicon-pixel and silicon-strip detectors, measures charged particle trajectories within the pseudorapidity range $|\eta| < 2.5$, where $\eta \equiv -\ln[\tan(\theta/2)]$ and θ is the polar angle of the trajectory of the particle with respect to the counterclockwise proton beam direction. A lead tungstate crystal electromagnetic calorimeter (ECAL), and a brass and scintillator hadron calorimeter (HCAL), each composed of a barrel and two endcap sections, provide energy measurements up to $|\eta| = 3$. Forward calorimeters extend the pseudorapidity coverage provided by the barrel and endcap detectors up to $|\eta| = 5$. Muons are identified and measured within the range $|\eta| < 2.4$ by gas-ionization detectors embedded in the steel magnetic flux-return yoke outside the solenoid. The detector is nearly hermetic, permitting the accurate measurement of $\vec{p}_{\mathrm{T}}^{\mathrm{miss}}$. A more detailed description of the CMS detector, together with a definition of the coordinate system used and the relevant kinematic variables, is given in Ref. [41].

3 Simulated event samples

The analysis makes use of several simulated event samples for modeling the SM background and signal processes. While the background estimation in the analysis is performed from control samples in the data, simulated event samples are used to propagate uncertainties as well as build understanding of the characteristics of the background events selected by this analysis.

The production of $\mathrm{t\bar{t}}$+jets, W+jets, Z+jets, and QCD multijet events is simulated with the Monte Carlo (MC) generator MADGRAPH5_aMC@NLO 2.2.2 [42] in leading-order (LO) mode. Single top quark events are modeled at next-to-leading order (NLO) with MADGRAPH5_aMC@NLO for the s-channel and POWHEG v2 [43, 44] for the t-channel and W-associated production. Additional small backgrounds, such as $\mathrm{t\bar{t}}$ production in association with bosons, diboson processes, and $\mathrm{t\bar{t}t\bar{t}}$ are similarly produced at NLO with either MADGRAPH5_aMC@NLO or POWHEG. All events are generated using the NNPDF 3.0 [45] set of parton distribution functions (PDF). Parton showering and fragmentation are performed with the PYTHIA 8.205 [46] generator with the underlying event model based on the CUETP8M1 tune detailed in Ref. [47]. The detector simulation is performed with GEANT4 [48]. The cross sections used to scale simulated event yields are based on the highest order calculation available.

Signal events for the TChiHH simplified model are generated for 33 values of the Higgsino mass between 200 GeV and 1000 GeV. The mass of the LSP (the Goldstino) is fixed to 1 GeV. The yields are normalized to the NLO + next-to-leading-logarithmic (NLL) cross section [36, 37]. The production cross sections are calculated assuming mass degeneracy for $\tilde{\chi}_1^0$, $\tilde{\chi}_2^0$, and $\tilde{\chi}_1^\pm$. All SUSY decays in the simplified model are taken to be prompt, though the lifetime of a true physical model would depend on the mass splitting between the Higgsino states and may be long-lived for very nearly degenerate states. Both Higgs bosons in each event are forced to decay to $b\bar{b}$, which is accounted for by scaling with the branching fraction. The events are generated in a manner similar to that for the SM backgrounds, with the MADGRAPH5_aMC@NLO 2.2.2

generator in LO mode using the NNPDF 3.0 PDF set and followed with PYTHIA 8.205 for showering and fragmentation. The detector simulation is performed with the CMS fast simulation package [49] with scale factors applied to account for differences with respect to the full simulation used for backgrounds.

Finally, to model the presence of additional proton-proton collisions from the same or adjacent beam crossing as the primary hard-scattering process ("pileup" interactions), the simulated events are overlaid with multiple minimum bias events, which are also generated with the PYTHIA 8.205 generator with the underlying event model based on the CUETP8M1 tune.

4 Event reconstruction and analysis variables

The reconstruction of physics objects in an event proceeds from the candidate particles identified by the particle-flow (PF) algorithm [50, 51], which uses information from the tracker, calorimeters, and muon systems to identify the candidates as charged or neutral hadrons, photons, electrons, or muons. Charged particle tracks are required to originate from the event primary vertex (PV), defined as the reconstructed vertex, located within 24 cm (2 cm) of the center of the detector in the direction along (perpendicular to) the beam axis, that has the highest value of p_{T}^2 summed over the associated charged particle tracks.

The charged PF candidates associated with the PV and the neutral PF candidates are clustered into jets using the anti-k_{T} algorithm [52] with distance parameter $R = 0.4$, as implemented in the FASTJET package [53]. The estimated pileup contribution to the jet p_{T} from neutral PF candidates is removed with a correction based on the area of the jet and the average energy density of the event [54]. The jet energy is calibrated using p_{T}- and η-dependent corrections; the resulting calibrated jet is required to satisfy $p_{\mathrm{T}} > 30\,\mathrm{GeV}$ and $|\eta| \leq 2.4$. Each jet must also meet loose identification requirements [55] to suppress, for example, calorimeter noise. Finally, jets that have PF constituents matched to an isolated lepton, as defined below, are removed from the jet collection.

A subset of the jets are "tagged" as originating from b quarks using DeepCSV [56], a new b-tagging algorithm based on a deep neural network [57]. The DeepCSV discriminator employs the same set of observables used by the combined secondary vertex (CSV) algorithm [58, 59], except that the track selection is expanded to include the leading six tracks, further improving the b-jet discrimination. In this analysis we use all three of the DeepCSV algorithm working points, loose, medium, and tight, defined as the values of the discriminator cut for which the rate for misidentifying a light-quark jet as a b jet are 10%, 1%, and 0.1%, respectively. The b-tagging efficiency for jets with p_{T} in the 50-150 GeV range is approximately 84%, 66% and 45% for the loose, medium and tight working points, respectively, and gradually decreases for lower and higher jet transverse momenta.

The missing transverse momentum, $p_{\mathrm{T}}^{\mathrm{miss}}$, is given by the magnitude of $\vec{p}_{\mathrm{T}}^{\mathrm{miss}}$, the negative vector sum of the transverse momenta of all PF candidates [50, 51]. Correspondence to the true undetectable energy in the event is improved by replacing the contribution of the PF candidates associated with a jet by the calibrated four-momentum of that jet. Filters are applied to reject events with well defined anomalous sources of $p_{\mathrm{T}}^{\mathrm{miss}}$ arising from calorimeter noise, beam halo, dead cells, and other effects.

Two types of lepton candidates are defined: *veto* leptons are used to suppress contamination from leptonic decays in the search region, while *signal* leptons are defined with tighter requirements and are used in the single-lepton and dilepton control regions. Electrons are reconstructed by associating a charged particle track with an ECAL supercluster [60]. Veto (signal) candidate electrons are required to have $p_{\mathrm{T}} > 10\,\mathrm{GeV}$ ($p_{\mathrm{T}} > 20\,\mathrm{GeV}$) and $|\eta| < 2.5$, and are required to satisfy identification criteria designed to minimize any misidentification of light-parton jets, photon conversions, and electrons from heavy flavor hadron decays as prompt electrons. Muons are reconstructed by associating tracks in the muon system with those found in the silicon tracker [61]. Veto (signal) muon candidates are required to satisfy $p_{\mathrm{T}} > 10\,\mathrm{GeV}$ ($p_{\mathrm{T}} > 20\,\mathrm{GeV}$) and $|\eta| < 2.4$.

To preferentially select leptons that originate in the decay of W and Z bosons, leptons are required to be isolated from other PF candidates. Isolation is quantified using an optimized version of the "mini-isolation" variable originally suggested in Ref. [62], in which the transverse energy of the particles within a cone in η-ϕ space surrounding the lepton momentum vector is computed using a cone size that scales with the inverse of the transverse momentum of the lepton. For more details on the precise definition of the lepton isolation used in this analysis, see Ref. [63] The combined efficiency for the signal electron reconstruction and isolation requirements is about 50% at a p_{T}^{ℓ} of 20 GeV, increasing to 65% at 50 GeV and reaching a plateau of 80% above 200 GeV. The combined reconstruction and isolation efficiencies for signal muons are about 70% at a p_{T}^{ℓ} of 20 GeV, increasing to 80% at 50 GeV and reaching a plateau of 95% at 200 GeV.

The dominant background in the analysis arises from the production of $\mathrm{t\bar{t}}$ single-lepton events in which the lepton is a τ decaying hadronically or is a light lepton that is not reconstructed or fails the lepton selection criteria, including the p_{T} threshold and the isolation requirements. To reduce this background, we veto events with any additional tracks corresponding to leptonic or hadronic PF candidates. To reduce the influence of tracks from extraneous pp interactions (pileup), isolated tracks are considered only if their nearest distance of approach along the beam axis to a reconstructed vertex is smaller for the primary event vertex than for any other vertex.

The requirements for the definition of an isolated track differ slightly depending on whether the track is identified as leptonic or hadronic by the PF algorithm. For leptonic tracks, we require $p_{\mathrm{T}} > 5\,\mathrm{GeV}$ and $I_{\mathrm{tk}} < 0.2$, where I_{tk} is the scalar p_{T} sum of other charged tracks within $\Delta R \equiv \sqrt{(\Delta\phi)^2 + (\Delta\eta)^2} < 0.3$ of the primary track, divided by the p_{T} value of the primary track. For hadronic tracks, we apply slightly tighter requirements to reduce hadronic (non-τ) signal loss: $p_{\mathrm{T}} > 10\,\mathrm{GeV}$ and $I_{\mathrm{tk}} < 0.1$. Since the isolation sum does not include neutral-particle candidates, the isolation distributions and efficiencies of leptonic tracks should be similar to those of pions from single-prong τ decays. To minimize the signal inefficiency due to this veto, isolated tracks are considered only if they satisfy

$$m_T(\mathrm{tk}, \vec{p}_{\mathrm{T}}^{\mathrm{miss}}) \equiv \sqrt{2 p_T^{\mathrm{tk}} p_{\mathrm{T}}^{\mathrm{miss}} [1 - \cos(\Delta\phi_{\mathrm{tk},\vec{p}_{\mathrm{T}}^{\mathrm{miss}}})]} < 100\,\mathrm{GeV}, \tag{1}$$

where p_T^{tk} is the transverse momentum of the track and $\Delta\phi_{\mathrm{tk},\vec{p}_{\mathrm{T}}^{\mathrm{miss}}}$ is the azimuthal separation between the track and $\vec{p}_{\mathrm{T}}^{\mathrm{miss}}$.

The majority of QCD multijet events in the high-$p_{\mathrm{T}}^{\mathrm{miss}}$ search region have jets with undermeasured momenta and thus a spurious momentum imbalance. A signature of such an event is a jet closely aligned in direction with the $\vec{p}_{\mathrm{T}}^{\mathrm{miss}}$ vector. To suppress this background, we place the following requirements on the angle $\Delta\phi_i$ between the i-th highest-p_{T} jet and $\vec{p}_{\mathrm{T}}^{\mathrm{miss}}$ for $i = 1, 2, 3, 4$: $\Delta\phi_1 < 0.5$, $\Delta\phi_2 < 0.5$, $\Delta\phi_3 < 0.3$, and $\Delta\phi_4 < 0.3$. No such requirement is placed on other jets.

The transverse hadronic energy H_{T} is defined as the scalar sum of the transverse momenta of the jets satisfying the criteria described above. Similarly, N_{jets} is the number of such jets, and $N_{\mathrm{b,L}}$, $N_{\mathrm{b,M}}$, and $N_{\mathrm{b,T}}$ the number of these jets tagged with the loose, medium, and tight b-tagging working points, respectively. By definition, the jets identified by each b-tagging working point form a subset of those satisfying the requirements of looser working points.

A single-lepton control sample is used to study the $\mathrm{t\bar{t}}$ background. To avoid possible signal contamination from SUSY processes leading to leptons, a maximum requirement is imposed on the transverse mass of these events:

$$m_{\mathrm{T}}(\ell, \vec{p}_{\mathrm{T}}^{\,\mathrm{miss}}) \equiv \sqrt{2 p_{\mathrm{T}}^{\ell} p_{\mathrm{T}}^{\mathrm{miss}} [1 - \cos(\Delta\phi_{\ell, \vec{p}_{\mathrm{T}}^{\,\mathrm{miss}}})]} < 100\,\mathrm{GeV}, \tag{2}$$

where $\Delta\phi_{\ell, \vec{p}_{\mathrm{T}}^{\,\mathrm{miss}}}$ is the difference between the azimuthal angles of the lepton momentum vector and the missing momentum vector, $\vec{p}_{\mathrm{T}}^{\,\mathrm{miss}}$.

To optimize signal efficiency and background rejection, we define the following mutually exclusive b-tagging categories:

- **2b category**: two tight b-tags ($N_{\mathrm{b,T}} = 2$, $N_{\mathrm{b,M}} = 2$),
- **3b category**: two tight b -tags and a medium b-tag ($N_{\mathrm{b,T}} \geq 2$, $N_{\mathrm{b,M}} = 3$, $N_{\mathrm{b,L}} = 3$), and
- **4b category**: two tight b-tags, a medium b-tag, and a loose b-tag ($N_{\mathrm{b,T}} \geq 2$, $N_{\mathrm{b,M}} \geq 3$, $N_{\mathrm{b,L}} \geq 4$).

The 2b category is used as a control sample to determine the kinematic shape of the background. Most of the signal events lie in the 3b and 4b categories. This categorization was found to have superior performance with respect to different combinations of working points. For instance, the simpler option of only using medium b-tags results in a loose 2b control sample that has a larger contribution from QCD, and a tight 4b sample with smaller signal efficiency.

To study various sources of background with higher statistical precision, we also define the following b-tag categories with looser requirements:

- **0b category**: no medium b-tags ($N_{\mathrm{b,M}} = 0$),
- **1b category**: one medium b-tags ($N_{\mathrm{b,M}} = 1$).

We will use N_{b} as a shorthand when discussing b-tag categories as an analysis variable, and $N_{\mathrm{b,L}}$, $N_{\mathrm{b,M}}$, and $N_{\mathrm{b,T}}$ when discussing numbers of b-tags for specific working points.

The principal visible decay products in signal events are the four b jets that arise from the decay of the two Higgs bosons. Additional jets may arise from initial-state radiation, final-state radiation or pileup. In order to reconstruct both Higgs bosons, we choose the four jets with the largest DeepCSV discriminator values, i.e., the four most b-like jets. These four jets can be grouped into three different pairs of Higgs boson candidates. Of the three possibilities, we choose the one with the smallest mass difference Δm between the two Higgs candidate masses m_{H_1}, m_{H_2}

$$\Delta m \equiv |m_{H_1} - m_{H_2}|\,. \tag{3}$$

This method exploits the fact that signal events contain two particles of identical mass, without using the known value of the mass itself. Methods that use the known mass to select the best candidate tend to sculpt an artificial peak in the background.

Only events where the masses of the two Higgs boson candidates are similar, $\Delta m < 40$ GeV, are kept. We then calculate the average mass as

$$\langle m \rangle \equiv \frac{m_{H_1} + m_{H_2}}{2}. \tag{4}$$

As discussed in Section 6, we define the Higgs boson mass window as $100 < \langle m \rangle \leq 140$ GeV.

After selecting the two Higgs boson candidates, we compute the distance ΔR between the two jets in each of the $\mathrm{H} \to \mathrm{b\bar{b}}$ candidate decays. We then define ΔR_{max} as the larger of these two values

$$\Delta R_{\mathrm{max}} \equiv \max\left(\Delta R_{H_1}, \Delta R_{H_2}\right). \quad (5)$$

In the typical configuration of signal events, ΔR_{max} is small because the Higgs bosons tend to have non-zero transverse boost and, thus, the two jets from the decay of a Higgs boson tend to lie near each other in η and ϕ. In contrast, for semileptonic $\mathrm{t\bar{t}}$ background events, three of the jets typically arise from a top quark that decays via a hadronically decaying W boson while the fourth jet arises from a b quark from the other top-quark decay. Therefore, three of the jets tend to lie within the same hemisphere while the fourth jet is in the opposite hemisphere. One of the Higgs boson candidates is thus formed from jets in both hemispheres, and ΔR_{max} tends to be larger than it is for signal events.

5 Trigger and event selection

The data sample used in this analysis was obtained with triggers that require the value of $p_{\mathrm{T}}^{\mathrm{miss}}$ to be greater than 100 GeV to 120 GeV, depending on the running period. This variable is computed with trigger-level quantities, and, as result, it has somewhat poorer resolution than the corresponding offline variable. The trigger efficiency, measured in samples triggered by a high-p_{T} isolated electron, rises rapidly from about 60% at $p_{\mathrm{T}}^{\mathrm{miss}} = 150$ GeV to over 99% for $p_{\mathrm{T}}^{\mathrm{miss}} > 300$ GeV. Systematic uncertainties on this efficiency are obtained by comparing the nominal trigger efficiency with that obtained in different kinematic regions, with different reference triggers, and with the simulation. This uncertainty is about 7% for $p_{\mathrm{T}}^{\mathrm{miss}} = 150$ GeV and decreases to 0.7% for $p_{\mathrm{T}}^{\mathrm{miss}} > 300$ GeV.

Several data control samples are employed to validate the analysis techniques and estimate systematic uncertainties on the background estimates. The control sample for the principal background from $\mathrm{t\bar{t}}$ events requires exactly one electron or one muon, while invisible Z boson decays are studied with a control sample requiring two leptons consistent with a $Z \to \ell\ell$ decay. These data samples were obtained with triggers that require at least one electron or muon with p_{T} greater than 27 GeV or 24 GeV, respectively.

Signal events have four b jets from the decay of two Higgs bosons with little or no additional hadronic activity and no isolated leptons. Thus, we select events with 4 or 5 jets, no veto leptons or isolated tracks, at least two tight b tags, $p_{\mathrm{T}}^{\mathrm{miss}} > 150$ GeV, high $\Delta\phi$, $\Delta m < 40$ GeV, and $\Delta R_{\mathrm{max}} < 2.2$. These selection requirements, listed in the top half of Table 1, are referred to as the *baseline selection*, while the bottom half of that table shows the further reduction in background in increasingly more sensitive search bins.

After the baseline selection, more than 85% of the remaining SM background arises from $\mathrm{t\bar{t}}$ production. The contributions from events with a W or Z boson in association with jets are about 10%. The background from QCD multijet events after the baseline selection is very small due to the combination of $p_{\mathrm{T}}^{\mathrm{miss}}$, $\Delta\phi$, and N_{b} requirements. The distributions of $\langle m \rangle$, Δm and ΔR_{max} in the 4b category are shown in Fig. 2 in data and simulation for illustration only. The background prediction is based on data control samples as described next.

As shown in Fig. 2, the $p_{\mathrm{T}}^{\mathrm{miss}}$ distribution of the signal is highly dependent on the Higgsino mass. Thus, to further enhance the sensitivity of the analysis we subdivide the search region into four $p_{\mathrm{T}}^{\mathrm{miss}}$ bins: $150 < p_{\mathrm{T}}^{\mathrm{miss}} \leq 200$ GeV, $200 < p_{\mathrm{T}}^{\mathrm{miss}} \leq 300$ GeV, $300 < p_{\mathrm{T}}^{\mathrm{miss}} \leq 450$ GeV,

Table 1: Event yields obtained from simulated event samples scaled to 35.9 fb^{-1}, as the event selection criteria are applied. The category "$\mathrm{t\bar{t}} + X$" is dominated by $\mathrm{t\bar{t}}$ (98.5%), but also includes small contributions from $\mathrm{t\bar{t}t\bar{t}}$, $\mathrm{t\bar{t}W}$, $\mathrm{t\bar{t}Z}$, $\mathrm{t\bar{t}H}$, and $\mathrm{t\bar{t}}\gamma$. The category "V+jets" includes Z+jets and W+jets in all their decays. The category "Other" includes ZZ, WZ, WW, WH($\to \mathrm{b\bar{b}}$), and ZH($\to \mathrm{b\bar{b}}$). The event selection requirements listed above the horizontal line in the middle of the table are defined as the *baseline selection*. The trigger efficiency is applied as an event weight and is first taken into account in the $p_{\mathrm{T}}^{\mathrm{miss}} > 150$ GeV row.

$\mathcal{L} = 35.9\ \mathrm{fb}^{-1}$	Other	Single t	QCD	V+jets	$\mathrm{t\bar{t}} + X$	Total SM bkg.	TChiHH (225,1)	TChiHH (400,1)	TChiHH (700,1)
No selection	–	–	–	–	–	–	10477.0	1080.4	84.0
0ℓ, 4-5 jets	–	–	–	–	–	–	4400.5	542.4	44.5
$N_{\mathrm{b,T}} \geq 2$	–	–	–	–	–	–	2479.4	304.2	23.8
$p_{\mathrm{T}}^{\mathrm{miss}} > 150$ GeV	122.3	1847.0	13201.4	2375.8	26797.7	44344.2±778.5	487.0	201.7	20.2
Track veto	91.4	1130.1	12251.8	1987.0	16910.1	32370.5±770.5	455.1	193.2	19.8
$\Delta\phi_{1,2} > 0.5, \Delta\phi_{3,4} > 0.3$	62.3	688.4	1649.0	1466.6	12027.0	15893.4±482.6	258.4	161.0	17.4
$\lvert\Delta m\rvert < 40$ GeV	35.9	366.0	831.9	745.5	7682.3	9661.6±440.8	187.1	118.9	12.0
$\Delta R_{\mathrm{max}} < 2.2$	14.2	138.2	147.0	336.9	3014.2	3650.5±90.2	95.1	80.1	9.9
$100 < \langle m \rangle \leq 140$ GeV	3.8	42.3	14.0	75.2	992.0	1127.3±10.1	70.4	61.1	8.1
3b + 4b	0.1	3.4	3.2	7.1	109.0	122.9±3.9	53.0	46.1	6.2
4b	0.1	0.7	3.2	1.5	27.3	32.8±3.4	35.4	32.0	4.4
$p_{\mathrm{T}}^{\mathrm{miss}} > 200$ GeV	0.1	0.3	3.2	1.1	9.4	14.1±3.3	15.0	26.2	4.2
$p_{\mathrm{T}}^{\mathrm{miss}} > 300$ GeV	0.0	0.1	0.0	0.4	1.1	1.7±0.2	2.4	11.6	3.4
$p_{\mathrm{T}}^{\mathrm{miss}} > 450$ GeV	0.0	0.0	0.0	0.1	0.1	0.1±0.1	0.1	1.1	1.9

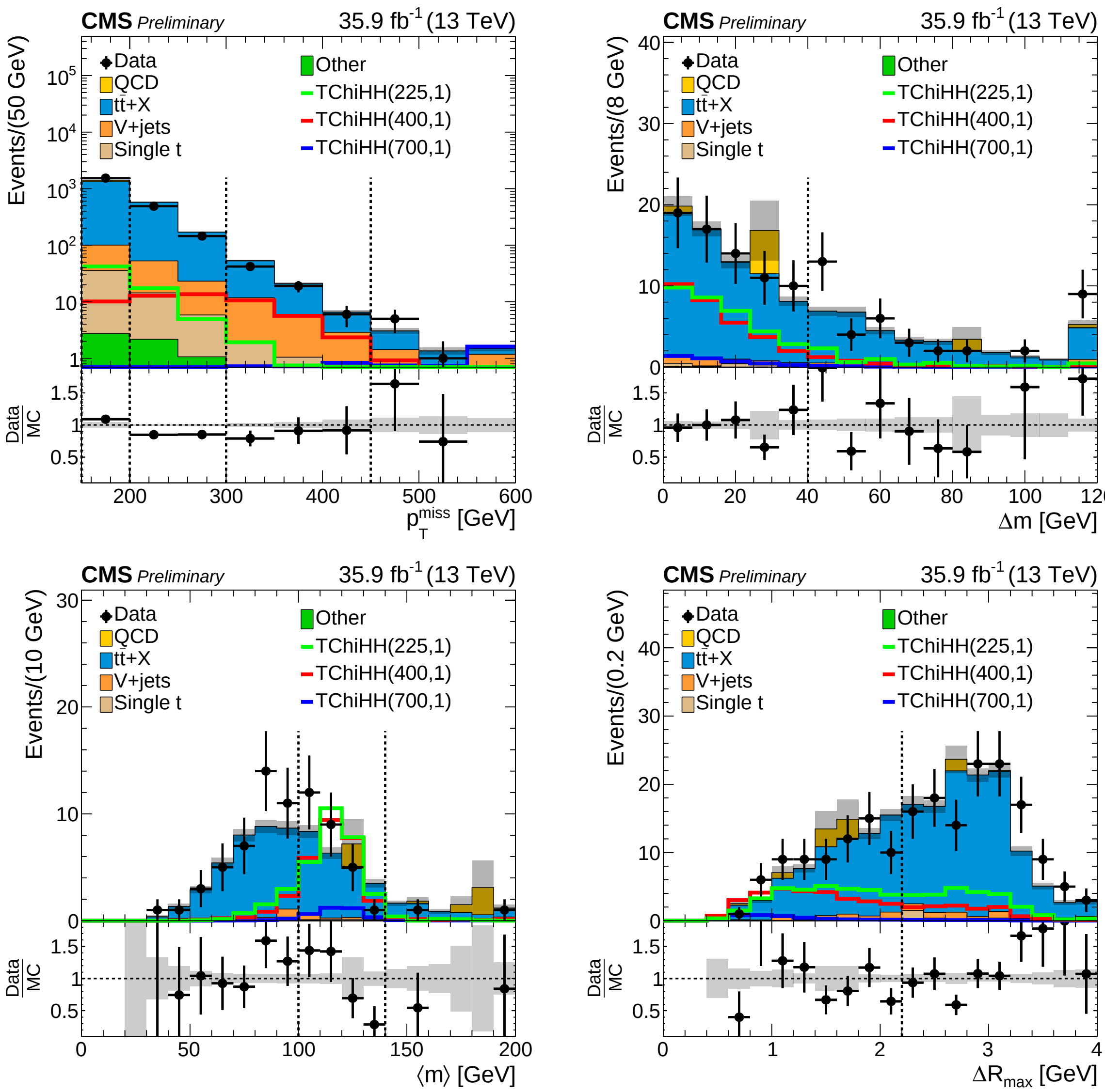

Figure 2: Distributions of $p_{\mathrm{T}}^{\mathrm{miss}}$, Δm, $\langle m \rangle$, and ΔR_{max} for data and simulated background samples, as well as signal benchmark points for three values of the Higgsino mass. All plots include baseline requirements, and the Δm, $\langle m \rangle$, and ΔR_{max} distributions also include the 4b selection. The simulation is normalized to the data yields. The gray shading indicates the statistical uncertainty on the total simulated background.

$p_{\mathrm{T}}^{\mathrm{miss}} > 450$ GeV. The background estimation procedure described in Section 6 is then applied simultaneously in each of the four $p_{\mathrm{T}}^{\mathrm{miss}}$ bins. Details of the background control samples will be given in Section 7 which covers the systematic uncertainties.

6 Background estimation

6.1 Method

The background estimation method is based on the observation that the $\langle m \rangle$ distribution is approximately uncorrelated with the number of b-tags. As shown in Fig. 3, the $\langle m \rangle$ shapes for the three event categories used in the analysis agree within the available statistics. This behavior can be understood by noting that the background in all three b-tag categories is dominated by

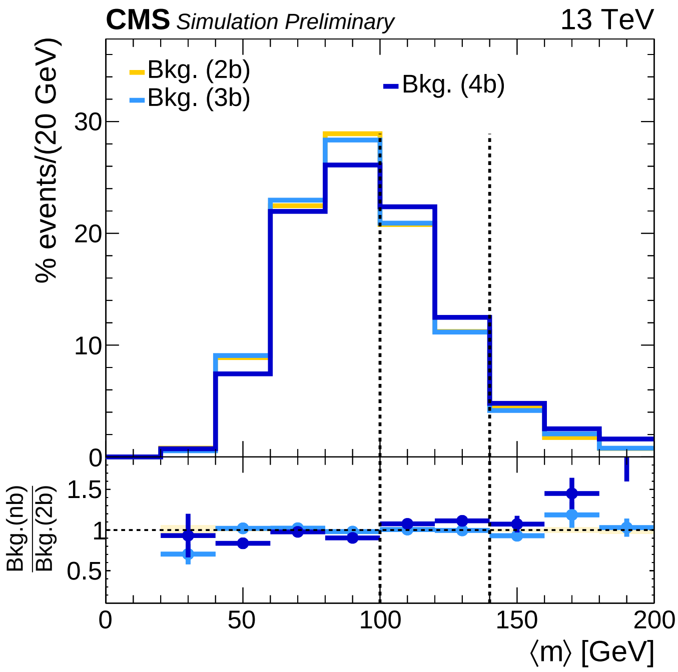

Figure 3: Comparison of the $\langle m \rangle$ shape from simulated background samples among the three b-tag categories after baseline selection. Note that QCD is not included due to the poor statistics of the simulation.

events containing only 2 b quarks, with the additional b-tagged jets in the 3b and 4b categories being mistagged light-quark or gluon jets. The background simulation indicates that less than 20% of the events in the 3b and 4b selection have more than 2 b quarks. As a result, the four jets used to construct $\langle m \rangle$ in the 3b and 4b categories have no distinct angular correlations as compared to the jets used to construct $\langle m \rangle$ in the 2b selection, and thus the shape of the average mass distribution is independent of N_{b} for $N_b \geq 2$.

Taking advantage of this observation, we construct an ABCD method [63] using $\langle m \rangle$ and the b-tag categories as the two dimensions. Specifically, we define the HIG region as the events with $\langle m \rangle$ within the Higgs boson mass window, 100 to 140 GeV, and the SBD region as the sum of all events outside the mass window up to $\langle m \rangle < 200$ GeV. The SBD and 2b regions are the sidebands, which are used to determine the background in the signal enriched HIG region for the 3b and 4b events independently for each $p_{\mathrm{T}}^{\mathrm{miss}}$ bin. In the limit that the b-tag category and $\langle m \rangle$ are uncorrelated, the background HIG / SBD ratio is the same for the three b-tag categories

$$\left(\frac{\mu^{\mathrm{bkg}}_{\mathrm{HIG}}}{\mu^{\mathrm{bkg}}_{\mathrm{SBD}}}\right)_{2\mathrm{b}} = \left(\frac{\mu^{\mathrm{bkg}}_{\mathrm{HIG}}}{\mu^{\mathrm{bkg}}_{\mathrm{SBD}}}\right)_{3\mathrm{b}} = \left(\frac{\mu^{\mathrm{bkg}}_{\mathrm{HIG}}}{\mu^{\mathrm{bkg}}_{\mathrm{SBD}}}\right)_{4\mathrm{b}} \equiv R_m, \tag{6}$$

where $\mu^{\mathrm{bkg}}_{n\mathrm{b,SBD}}$ and $\mu^{\mathrm{bkg}}_{n\mathrm{b,HIG}}$ are the estimated (Poisson) means of the background for each b-tag category ($n = 2, 3, 4$) in the SBD and HIG search regions, respectively. The resulting background predictions are

$$\mu^{\mathrm{bkg}}_{3\mathrm{b,HIG}} = \mu^{\mathrm{bkg}}_{3\mathrm{b,SBD}} \times R_m \quad \text{and} \quad \mu^{\mathrm{bkg}}_{4\mathrm{b,HIG}} = \mu^{\mathrm{bkg}}_{4\mathrm{b,SBD}} \times R_m. \tag{7}$$

The *closure* of the background estimation method, that is, the ability of Eq. 7 to predict the

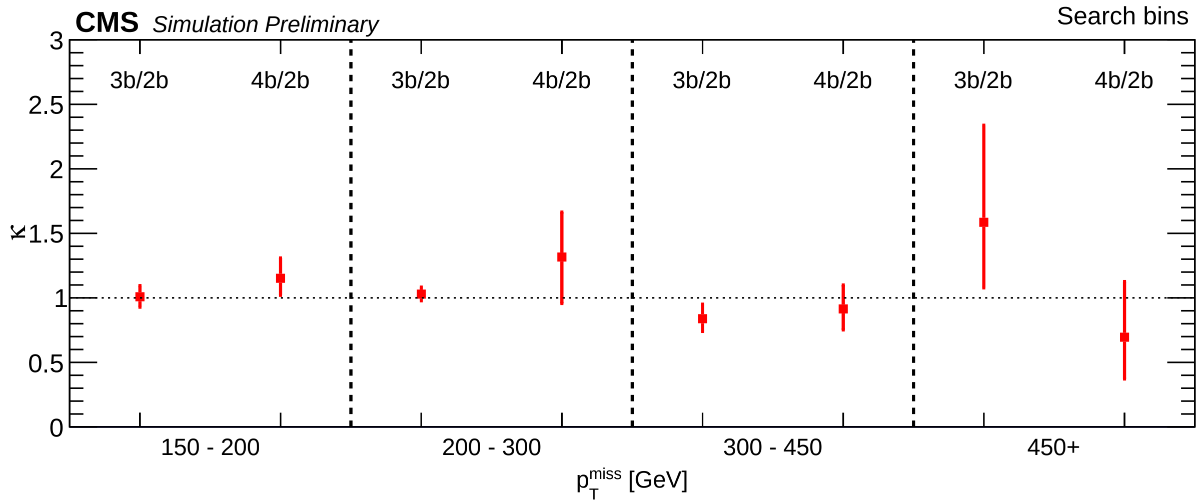

Figure 4: Values of the double-ratios κ_{3b} and κ_{4b} obtained from the background simulation for each of the p_T^{miss} bins.

background rates in the signal regions, is quantified with the double ratio κ

$$\kappa_{nb} = \left(\frac{\mu^{bkg}_{HIG}}{\mu^{bkg}_{SBD}}\right)_{nb} \Big/ \left(\frac{\mu^{bkg}_{HIG}}{\mu^{bkg}_{SBD}}\right)_{2b}. \tag{8}$$

These κ factors measure the impact of any residual correlation between the b-tag category and $\langle m \rangle$. Figure 4 shows that the κ factors in simulation are consistent with unity for both the 3b and 4b regions across the full p_T^{miss} range, demonstrating the fundamental assumption of the ABCD method. In Section 7, we study the closure of the method in data control samples and estimate the associated systematic uncertainties on the background prediction.

6.2 Implementation

The method outlined in Section 6.1 is implemented with a likelihood function that incorporates the systematic uncertainties on the closure and accounts for signal contamination in the $\langle m \rangle$ SBD and 2b sideband regions.

The likelihood function is the product of Poisson probability density functions, one for each observable, given by

$$\mathcal{L} = \mathcal{L}^{data}_{ABCD} \cdot \mathcal{L}^{MC}_{sig}, \tag{9}$$

$$\begin{aligned}\mathcal{L}^{data}_{ABCD} = &\prod_{m=1}^{4}\prod_{n=2}^{4} \text{Poisson}(N^{data}_{nb,SBD,m} | \mu^{bkg}_{nb,SBD,m} + r \cdot \mu^{MC,sig}_{nb,SBD,m}) \times \\ &\prod_{m=1}^{4}\prod_{n=2}^{4} \text{Poisson}(N^{data}_{nb,HIG,m} | \mu^{bkg}_{nb,SBD,m} \times R_m + r \cdot \mu^{MC,sig}_{nb,HIG,m}),\end{aligned} \tag{10}$$

$$\mathcal{L}^{MC}_{sig} = \prod_{m=1}^{4}\prod_{n=2}^{4} \text{Poisson}(N^{MC,sig}_{nb,SBD,m} | \mu^{MC,sig}_{nb,SBD,m}) \times \prod_{m=1}^{4}\prod_{n=2}^{4} \text{Poisson}(N^{MC,sig}_{nb,HIG,m} | \mu^{MC,sig}_{nb,HIG,m}), \tag{11}$$

where N^{data} and N^{MC} refer to the observed number of events in data and the simulation, $\mu^{MC,sig}_{nb}$ is the expected number of signal events, and r is the strength of the signal. For each p_T^{miss} bin m, there are four main floating parameters describing the fitted background rates: the three sideband background rates $\mu^{bkg}_{nb,SBD,m}$ and the ratio R_m.

In Eq. (9), $\mathcal{L}^{\text{data}}_{\text{ABCD}}$ accounts for the statistical uncertainty in the observed data yields in each of the 4×6 regions, and $\mathcal{L}^{\text{MC}}_{\text{sig}}$ accounts for the uncertainty in the computation of the signal shape due to the finite size of the MC samples.

The systematic uncertainties on the closure and the signal efficiency are described in the following sections. These effects are incorporated in the likelihood function as log-normal constraints multypling the event rates with a nuisance parameter for each uncorrelated source of uncertainty. These terms are not explicitly shown in the likelihood function above for simplicity.

The likelihood function defined in Eqs. (9)–(11) is employed in two separate types of fits that provide complementary but compatible background estimates based on an ABCD model. The first type of fit, which we call the *predictive fit*, allows us to more easily establish the agreement of the background predictions and the observations in the null (i.e., the background-only) hypothesis. We do this by excluding the observations in the signal regions in the likelihood (that is, by not including the (3b,HIG) and (4b,HIG) bins in the products of Eq. (10)) and fixing the signal strength r to 0. This procedure leaves as many unknowns as constraints: four *data* floating parameters ($\mu^{\text{bkg}}_{\text{2b,SBD}}$, $\mu^{\text{bkg}}_{\text{3b,SBD}}$, $\mu^{\text{bkg}}_{\text{4b,SBD}}$, and R_m) and four observations ($N^{\text{data}}_{\text{2b,SBD}}$, $N^{\text{data}}_{\text{3b,SBD}}$, $N^{\text{data}}_{\text{4b,SBD}}$, and $N^{\text{data}}_{\text{2b,HIG}}$) for each $p_{\text{T}}^{\text{miss}}$ bin. In the likelihood function there are additional floating parameters associated with the signal yields, which have small uncertainties. As a result, the estimated background rates in the control regions converge to the observed values in those bins, and we obtain predictions for the signal regions that do not depend on the observed $N^{\text{data}}_{\text{3b,HIG}}$ and $N^{\text{data}}_{\text{4b,HIG}}$ yields. The predictive fit thus converges to the standard ABCD method, and the likelihood machinery becomes just a convenient way to solve the system of equations and propagate the various uncertainties.

Additionally, we implement a *global fit* which, by making use of the observations in the signal regions, can provide an estimate of the signal strength r, while allowing for signal events to populate the control regions. This is achieved by including all $N^{\text{data}}_{n\text{b,SBD}}$ and $N^{\text{data}}_{n\text{b,HIG}}$ observations, ($n = 2, 3, 4$), in the likelihood function. Since there are six observations and four floating background parameters in each ABCD plane, there are enough constraints for the signal strength also to be determined in the fit.

7 Systematic uncertainties

7.1 Overview

The background estimation procedure described in Section 6 relies on the approximate independence of the $\langle m \rangle$ and N_{b} distributions. The closure of the method for each signal bin can be quantified with the double-ratio κ (Eq. 8), expected to be unity in the case of $\langle m \rangle$ and N_{b} being uncorrelated. In the simulation, the κ factors are close to 1 (Fig. 4) because the following two conditions are approximately true:

1. The distributions of $\langle m \rangle$ and N_{b} are independent for each background category.

2. The relative abundance of each background component is independent of N_{b}.

These conditions are sufficient to ensure that the overall κ is unity, even when each background has different $\langle m \rangle$ shape (which is the case for the two main backgrounds, $\text{t}\bar{\text{t}}$ and Z+jets). In this section, we present the data control sample studies that test these expectations together with the resulting estimates for the systematic uncertainties on the closure of the background estimate method for each search bin.

In Sections 7.2, 7.3, and 7.4, we study the first condition by defining dedicated data control regions for $t\bar{t}$, Z+jets and QCD multijet production and examining the closure of the background estimation method for each of these individual background processes in the data. Then, in Section 7.5, we use these data control samples to quantify the validity of the simulation prediction that the background admixture is independent of N_b in each p_T^{miss} bin, the second closure condition, by examining the modeling of the p_T^{miss} and N_b distributions for each background source. Finally, Section 7.6 describes the prescription for combining the findings based on these data control sample studies into a total systematic uncertainty on the background prediction in each search bin.

7.2 Single-lepton $t\bar{t}$ control sample

To test whether the background estimation method works for $t\bar{t}$-like processes, we define a single lepton control sample, which, like the search region, is dominated by single lepton $t\bar{t}$ events and represents a similar kinematic phase space. Since the lepton is a spectator object as far as the ABCD method is concerned —it is neither involved in the construction of the $\langle m \rangle$ variable, nor correlated with the presence of additional b-jets— this control sample should accurately capture any potential mismodeling of the $\langle m \rangle$-N_b correlation that may be present in the signal region.

For each of the 6 nominal ABCD planes, we construct a corresponding single-lepton ABCD plane, where all cuts are kept the same except for removing the lepton and isolated track vetoes and instead requiring exactly one signal lepton with $p_T > 30$ GeV (to reach trigger plateau) and $m_T < 100$ GeV (to avoid poorly reconstructed events and possible signal contamination from other SUSY models). Given that the single lepton region is free of QCD contamination, the $\Delta\phi$ cut is also removed. Since the presence of the lepton allows us to trigger on events with lower p_T^{miss}, we add two additional p_T^{miss} bins, $p_T^{miss} < 75$ GeV and $75 < p_T^{miss} \leq 150$ GeV, allowing to study the p_T^{miss} dependence of the closure in a wider range. Except for the $p_T^{miss} > 300$ GeV bin where the contribution of single top production and V+jets can be altogether as high as $\sim$25%, $t\bar{t}$ accounts for over 90% of the events in this control region. Data-to-simulation comparison shows good agreement for the $\langle m \rangle$ distribution, as seen in Figure 5 (left), as well as for the other Higgs reconstruction variables, Δm and ΔR_{max}.

As described in Section 6, since the 3b and 4b categories are dominated by events with two true B hadrons and one or two additional mistagged jets, similar jet topologies contribute to all b-tag categories and thus the $\langle m \rangle$ distributions of the reconstructed b-tag categories converge. We validate this assertion in the single-lepton control sample by examining the value of the κ factor. Figure 6 shows the overall closure of the method in bins of p_T^{miss} both in the simulation and in data. We observe good closure within the statistical uncertainties. As expected from the simulation, the data κ values are consistent with unity across the full p_T^{miss} range.

To assign the final uncertainty on the closure of the method in $t\bar{t}$-like events, we take advantage of the fact that the closure of the method is not expected to depend on p_T^{miss}. This is confirmed within the available data and simulation statistics, shown in Fig. 6, as well as after loosening the selection by removing the ΔR_{max} cut. Additionally, from simulation we know that the true B-hadron composition of each b-tag category does not depend on p_T^{miss}. We thus integrate over p_T^{miss} to increase the statistical precision of the closure test and assign the larger of the non-closure and the statistical uncertainty as the systematic uncertainty on the closure of the method in $t\bar{t}$-like events. The results, shown to the right of the solid line in Fig. 6 correspond to an uncertainty of 3% and 6% in the 3b and 4b bins, respectively.

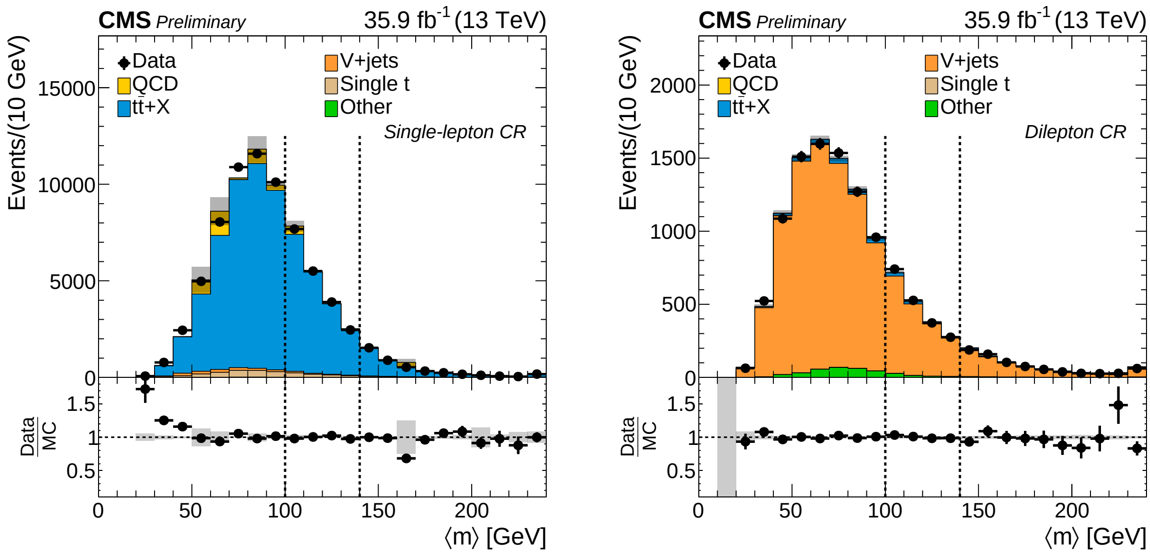

Figure 5: Comparison of the distribution of $\langle m \rangle$ in data and simulation in the single-lepton control sample (left) and the dilepton control sample (right) integrated in $p_{\mathrm{T}}^{\mathrm{miss}}$. The simulation is normalized to the data yields. The gray shading indicates the statistical uncertainty on the total simulated background.

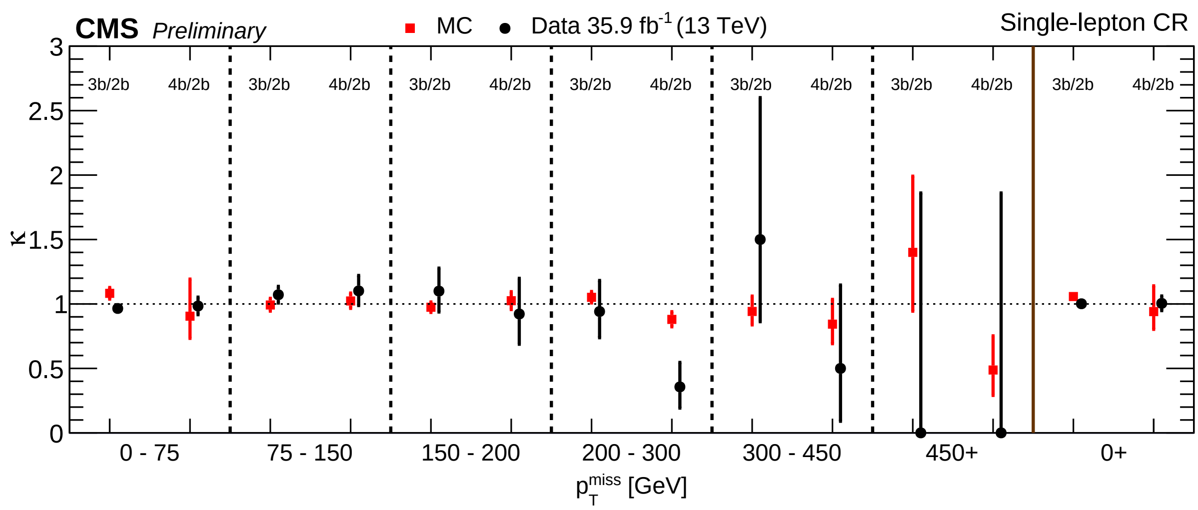

Figure 6: Comparison of the κ values found in the single-lepton control sample, for data and simulated events, for the 2b-3b and 2b-4b ABCD planes in each $p_{\mathrm{T}}^{\mathrm{miss}}$ bin.

7.3 Z+jets control sample

As shown in Section 5, the second largest background is Z+jets, with the Z boson decaying as $Z \to \nu\nu$. Similarly to the $t\bar{t}$ case, we can validate the background estimation method for Z+jets events by constructing a closure test in a representative data control sample rich with $Z \to \ell\ell$ decays. However, given the small branching fraction of $Z \to \ell\ell$ decays and the large $t\bar{t}$ contamination associated with a high N_b selection, we test the method by constructing ABCD planes with lower b-tag requirements, namely 1b/0b and 2b/1b. The additional 0b and 1b categories are selected by requiring exactly 0 and 1 medium b-tags, respectively.

The $Z \to \ell\ell$ control sample is constructed in a similar manner to the search region. Events with 4 or 5 jets are selected, and the double-Higgs-boson reconstruction proceeds as described in Section 4. We require two opposite-sign same-flavor signal leptons in the Z-mass window, $80 < m(\ell\ell) \leq 100$ GeV, with the p_T of the leading lepton being greater than 40 GeV due to trigger constraints. We remove the lepton and isolated track vetoes and, since the dilepton requirement makes the contamination from QCD events negligible, we remove the $\Delta\phi$ cut. Since we do not expect real p_T^{miss} from the targeted DY+jets events, we additionally require $p_T^{miss} < 50$ GeV, which reduces the contamination of other processes from 20% to 10%.

We divide the sample in bins of $p_T(\ell\ell)$, ensuring kinematic correspondence with the $Z \to \nu\nu$ decays present in the various p_T^{miss} bins employed in the search region. Similarly to the single-lepton sample, the presence of leptons allows us to study the closure for lower values of $p_T(\ell\ell)$ as well. Figure 5 (right) shows both the high purity of the sample and the excellent data to simulation agreement in the $\langle m \rangle$ shape.

The validity of the extrapolation of the method to a sample consisting of lower b-tag multiplicities is supported by the observation that all jets in V+jets events come from ISR, and thus their kinematic properties are largely independent of the flavor content of the event. This expectation is confirmed in data by examining the overall closure of the method in bins of $p_T(\ell\ell)$ as seen in Fig. 7, where the values of κ found in the simulation and data are compared to unity.

Since we do not observe that the closure of the method has any dependence on $p_T(\ell\ell)$, we proceed to combine all the $p_T(\ell\ell)$ bins into one bin to the right of the solid brown line and repeat the closure test with improved statistical precision. The 1b/0b test shown in Fig. 7 shows a residual non-closure of 11%, which may be due to higher order effects beyond the precision of this search. A similar 2b/1b test shows good closure but with a higher statistical uncertainty of 19%. We proceed to assign the larger uncertainty of 19% as the systematic uncertainty on the closure of the background estimate method for Z+jets events. The robustness of this result is further corroborated by similar checks in a looser selection, without the ΔR_{max} cut.

7.4 Systematic uncertainty on the QCD contribution

The systematic uncertainty for the QCD background is set by following the same procedure as for the Z+jets background. Namely, we define a QCD-enriched control region by inverting the $\Delta\phi$ cut. Then, since the high b-tag multiplicity region of the control sample has limited event yield and high $t\bar{t}$ contamination, we check the $\langle m \rangle$-N_b independence in lower b-tag multiplicity regions, the 1b/0b and 2b/1b ABCD planes. Due to the strong QCD supression at high p_T^{miss} and high N_b, the purity of this sample in the lowest p_T^{miss} bin ranges from 87% to 67% with increasing N_b. At high p_T^{miss}, the sample becomes dominated by Z+jets and $t\bar{t}$ at low and high N_b, respectively.

Similarly, to the previous control regions we observe good agreement in the data-to-simulation comparison in $\langle m \rangle$ and, since there is no expected p_T^{miss} dependence and a higher purity at

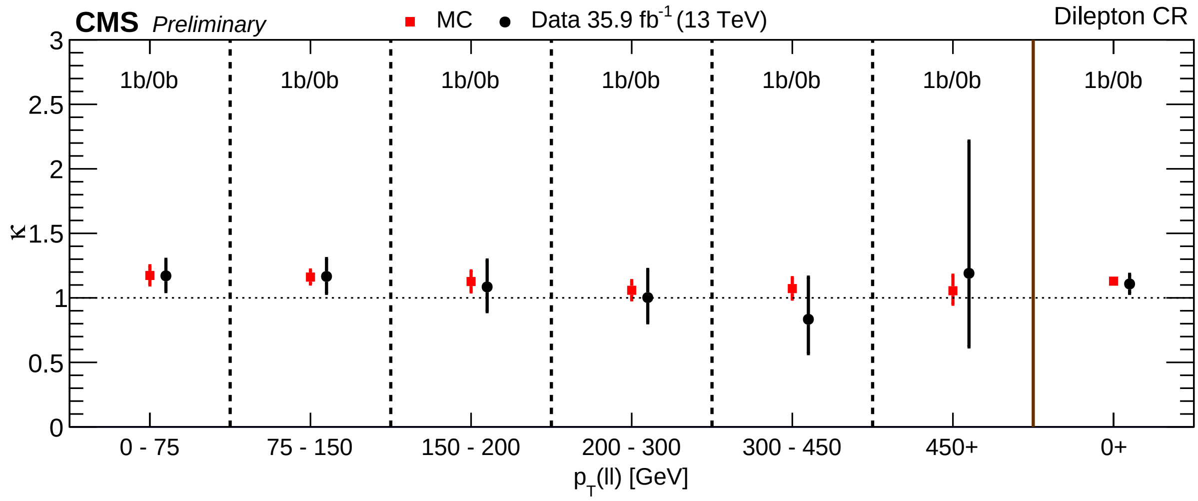

Figure 7: Comparison of the κ values found in the dilepton control sample, data and simulation, for the 1b/0b ABCD planes in bins of $p_T(\ell\ell)$.

low $p_{\mathrm{T}}^{\mathrm{miss}}$, we proceed to quantify the closure of the method after integrating in $p_{\mathrm{T}}^{\mathrm{miss}}$. Having examined both the 1b/0b and 2b/1b ABCD planes, with and without the ΔR_{max} cut, we observe a maximum deviation of κ of 13%, which we assign as the systematic uncertainty on the closure of the background estimate method for QCD events.

7.5 Impact of the background composition

Having evaluated the closure of the method for each individual background, we proceed to study the impact of mismodeling the relative abundance of the different background sources.

Since the $\langle m \rangle$ shape varies between background types as seen in Fig. 5, differences in the process admixture in the 2b category vs the 3b or 4b categories will result in $\langle m \rangle$-N_{b} correlation and lead to non-closure of the method. From simulation, the background composition is expected to be independent of the b-tag category. The validity of this prediction relies on the ability of the simulation to model the shape of the b-tag category distribution equally well for each background. As an example, if a particular background has a harder N_{b} distribution than predicted in simulation, while the N_{b} shape is well modeled for other backgrounds, then the relative abundance of the mismodeled background would be underestimated, distorting the total $\langle m \rangle$ shape at high N_{b}. The final impact of such an effect in each bin will also be modulated by the abundance of each background and therefore also relies on the modeling of the $p_{\mathrm{T}}^{\mathrm{miss}}$ spectrum for each background.

Data-to-simuation comparisons show that the N_{b} distribution is indeed similarly modeled for $\mathrm{t\bar{t}}$, Z+jets and QCD multijet production. The $p_{\mathrm{T}}^{\mathrm{miss}}$ distribution in simulation is found to overestimate the data for large values of $p_{\mathrm{T}}^{\mathrm{miss}}$ for $\mathrm{t\bar{t}}$ and Z+jets events, while the opposite is observed for QCD multijet events. To provide an estimate of the potential impact of mismodeling of the composition on the closure, we reweight the simulation using the data/MC comparisons and then calculate the κ factors using the reweighted simulation, proceeding to assign 100% of the shift in their values with respect to the nominal simulation as the uncertainty on the modeling of the background composition. This test is performed after integrating 3b and 4b, and loosening the $\Delta\phi$ cut (requiring $\phi_1 > 0.3$ and $\phi_2 > 0.3$), in order to allow some QCD events to be selected so that the propagation of the effect of the QCD on the total background is meaningful. The resulting uncertainty is found to be within 4%.

7.6 Total systematic uncertainty determination

As described in Sections 7.2, 7.3, 7.4, and 7.5, we define individual data control regions for $t\bar{t}$, Z+jets and QCD multijet production where we study the closure of the background estimation method for each of these background processes in the data and validate the simulation prediction that κ is consistent with unity for each of these backgrounds within the precision of this analysis. We perform these studies in various looser selections to examine the ability of the simulation to predict the closure of the method at high $p_{\mathrm{T}}^{\mathrm{miss}}$ with better statistical precision. We then use the data control regions to understand the modeling of the N_{b} and $p_{\mathrm{T}}^{\mathrm{miss}}$ distributions for each background, which directly translates into quantifying the ability of the simulation to predict the relative abundance of the backgrounds in each search bin.

Finally, we employ these data control sample studies to assign a set of systematic uncertainties on the overall κ for each search bin as follows:

1. The closure uncertainty for each background process obtained in data CRs is propagated to the overall κ by varying the closure of the particular background in simulation in bins of $p_{\mathrm{T}}^{\mathrm{miss}}$ and N_{b}. The resulting shifts of the κ factors, ranging from 1% to 10% increasing with $p_{\mathrm{T}}^{\mathrm{miss}}$, are assigned as systematic uncertainties with a 100% bin-to-bin correlation.

2. The level of non-closure due to the relative abundance of each background component as a function of N_{b} is estimated by comparing the change in κ in simulation before and after correcting the N_{b} and $p_{\mathrm{T}}^{\mathrm{miss}}$ distributions of each background source according to measurements in the data control samples. Its overall impact is 1–4% and it is taken as 100% correlated across the different analysis bins.

3. Since there are no known sources of $p_{\mathrm{T}}^{\mathrm{miss}}$ dependence that are significant within the context of the available data sample and no $p_{\mathrm{T}}^{\mathrm{miss}}$ dependence is observed in the data, the closure uncertainties for each background process derived in data are integrated in $p_{\mathrm{T}}^{\mathrm{miss}}$. Instead, having extensively validated the ability of the simulation to model both the closure of the method for the individual backgrounds and the relative admixture of the backgrounds in each search bin, we take the larger of the statistical uncertainty and the non-closure for each bin in the simulation as the systematic uncertainty on the closure of the method as a function of $p_{\mathrm{T}}^{\mathrm{miss}}$ and N_{b}. As seen in Fig. 4, this uncertainty ranges from 8–15% in the lowest $p_{\mathrm{T}}^{\mathrm{miss}}$ bin to 59–75% in the highest-$p_{\mathrm{T}}^{\mathrm{miss}}$ bin, and is assumed to be uncorrelated between bins.

Due to the robustness of the background method, evidenced by the high-statistics data CR studies integrated in $p_{\mathrm{T}}^{\mathrm{miss}}$, the final uncertainty is dominated by the statistical precision of the simulation in evaluating the closure as a function of $p_{\mathrm{T}}^{\mathrm{miss}}$, described in the third item. Nevertheless, each of the listed uncertainties is incorporated in the background fit as a log-normal constraint in the likelihood function as described in Section 6.2, taking into account the stated correlations.

8 Results and interpretation

The observed event yields in data and the total predicted SM background are listed in Table 2, along with the expected yields for three Higgsino-mass scenarios. Two background estimates are given: the predictive fit, which does not use the data in the signal regions and ignores signal contamination in the other regions, and the global fit, which also incorporates the observations in the (HIG,3b) and (HIG,4b) regions, as described in Section 6.2. Since we observed 0 events

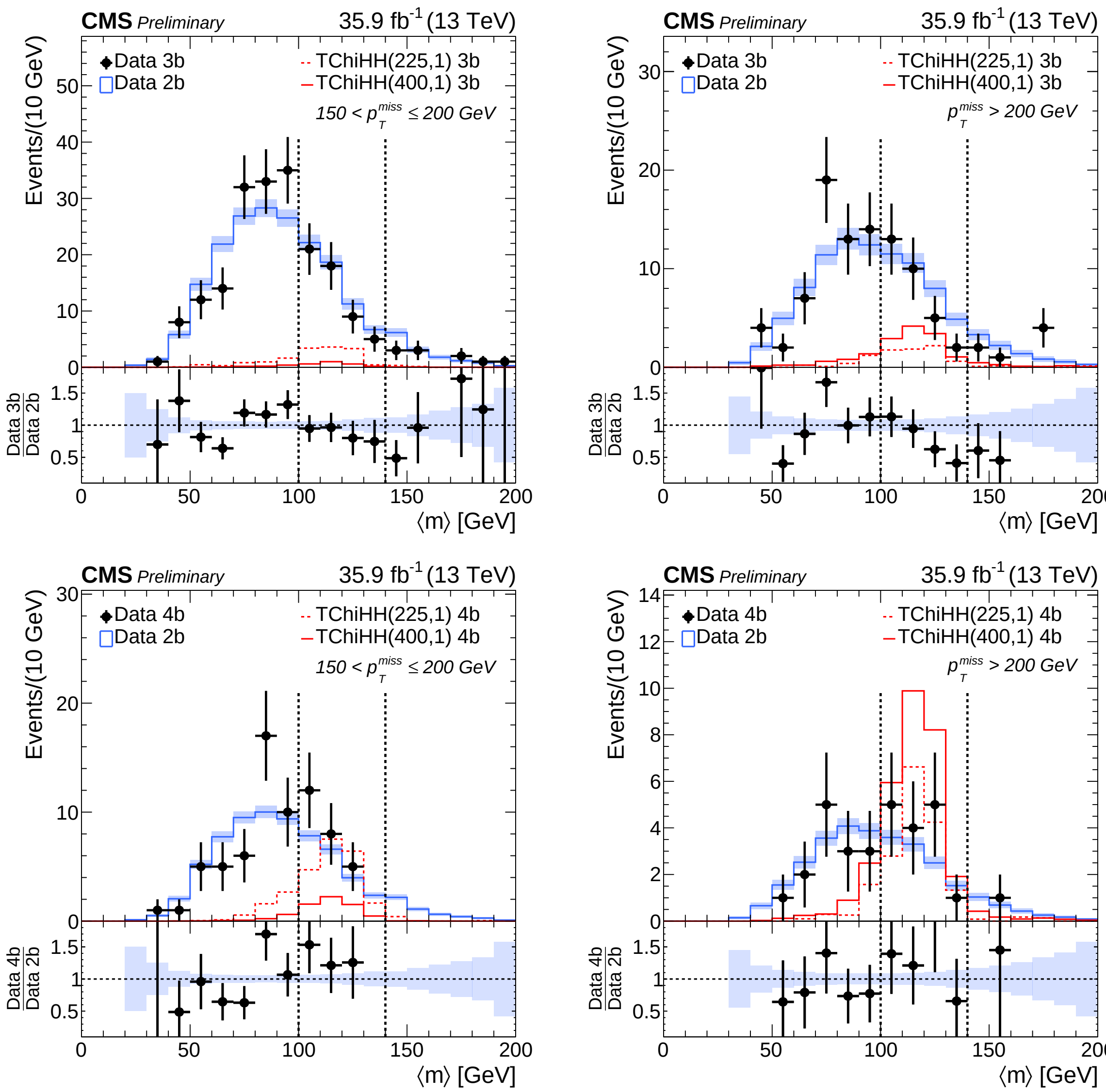

Figure 8: Distributions of $\langle m \rangle$ in data and two signal benchmark models. The points with error bars show the data in the 3b (top) and 4b bins (bottom) for $150 < p_{\mathrm{T}}^{\mathrm{miss}} \leq 200$ GeV (left) and $p_{\mathrm{T}}^{\mathrm{miss}} > 200$ GeV (right). The histograms show the shape of the $\langle m \rangle$ distribution observed in the 2b bin with an overall event yield normalized to those observed in the 3b and 4b samples. The shaded areas reflect the statistical uncertainty on the $\langle m \rangle$ distribution in the 2b data. The ratio plots demonstrate that the shapes are in agreement.

in the (SBD, 4b) region, the parameter $\mu^{\mathrm{bkg}}_{\mathrm{4b,SBD}}$ is fitted to be 0, pushing against its physical boundary and leading to the underestimation of the associated uncertainty. We account for this by including an additional uncertainty that makes the uncertainty on $\mu^{\mathrm{bkg}}_{\mathrm{4b,SBD}}$ consistent with having observed 1 event. In all cases, the event yields observed in data are consistent with the predictions within 2σ, and no pattern of deviations is evident.

Figure 8 shows the distributions in data of $\langle m \rangle$ in the 3b and 4b bins for $150 < p_{\mathrm{T}}^{\mathrm{miss}} \leq 200$ GeV and $p_{\mathrm{T}}^{\mathrm{miss}} > 200$ GeV. In each plot, the renormalized histogram of the $\langle m \rangle$ distribution in the 2b bin is overlaid for comparison. The shapes of the $\langle m \rangle$ distributions are consistent. The signal region (HIG) in $\langle m \rangle$ lies between the two vertical dotted lines, and no significant excess is observed, in either the 3b or in the 4b bins.

Table 2: Observed event yields ("Obs.") for all control and signal regions in each of the four $p_{\mathrm{T}}^{\mathrm{miss}}$ bins corresponding to 35.9 fb^{-1} of data. The predicted SM background rates ("Pred.") in the (HIG,3b) and (HIG,4b) regions correspond to the values obtained with the predictive fit. The results of the global fit under the background-only hypothesis ($r = 0$) are also shown. The expected signal yields for three values of the Higgsino mass are shown for reference.

$\mathcal{L} = 35.9\ \mathrm{fb}^{-1}$	Global fit	Pred.	Obs.	TChiHH (225,1)	TChiHH (400,1)	TChiHH (700,1)
$150 < p_{\mathrm{T}}^{\mathrm{miss}} \leq 200$ GeV						
SBD, 2b	$1560.1^{+39.7}_{-38.5}$		1559	5.9	1.0	0.0
HIG, 2b	$656.2^{+25.2}_{-24.6}$		658	10.5	2.7	0.1
SBD, 3b	$140.3^{+10.8}_{-10.3}$		145	4.6	1.0	0.0
HIG, 3b	$57.7^{+5.5}_{-5.2}$	$61.2^{+8.4}_{-7.7}$	53	10.7	2.3	0.1
SBD, 4b	$48.1^{+6.4}_{-5.8}$		45	5.4	1.1	0.0
HIG, 4b	$21.9^{+3.5}_{-3.2}$	$19.0^{+4.6}_{-3.9}$	25	20.3	5.8	0.3
$200 < p_{\mathrm{T}}^{\mathrm{miss}} \leq 300$ GeV						
SBD, 2b	$588.0^{+24.2}_{-23.5}$		585	2.5	3.4	0.1
HIG, 2b	$333.1^{+17.9}_{-17.6}$		336	6.2	6.6	0.3
SBD, 3b	$55.3^{+6.5}_{-5.9}$		61	2.2	2.6	0.1
HIG, 3b	$30.6^{+3.9}_{-3.6}$	$35.1^{+5.9}_{-5.5}$	25	5.7	6.5	0.3
SBD, 4b	$15.6^{+3.8}_{-3.1}$		13	2.5	2.9	0.1
HIG, 4b	$11.4^{+3.0}_{-2.5}$	$7.5^{+3.8}_{-2.7}$	14	12.6	14.4	0.8
$300 < p_{\mathrm{T}}^{\mathrm{miss}} \leq 450$ GeV						
SBD, 2b	$72.4^{+8.7}_{-8.1}$		74	0.1	2.0	0.2
HIG, 2b	$40.6^{+6.3}_{-6.0}$		39	0.6	5.0	0.6
SBD, 3b	$5.7^{+2.2}_{-1.8}$		4	0.1	1.7	0.1
HIG, 3b	$3.3^{+1.4}_{-1.1}$	$2.1^{+1.4}_{-1.0}$	5	0.6	4.6	0.5
SBD, 4b	$1.9^{+1.4}_{-0.9}$		2	0.1	1.9	0.2
HIG, 4b	$1.1^{+0.8}_{-0.5}$	$1.1^{+1.0}_{-0.6}$	1	2.3	10.4	1.5
$p_{\mathrm{T}}^{\mathrm{miss}} > 450$ GeV						
SBD, 2b	$5.4^{+2.5}_{-2.1}$		5	0.0	0.2	0.2
HIG, 2b	$4.6^{+2.2}_{-1.9}$		5	0.0	0.6	0.9
SBD, 3b	$0.6^{+0.8}_{-0.4}$		1	0.0	0.1	0.2
HIG, 3b	$0.4^{+0.6}_{-0.3}$	$1.0^{+1.6}_{-1.0}$	0	0.0	0.4	0.7
SBD, 4b	$0.0^{+0.3}_{-0.0}$		0	0.0	0.2	0.2
HIG, 4b	$0.0^{+0.3}_{-0.0}$	$0.0^{+1.2}_{-0.0}$	0	0.1	1.1	1.9

Table 3: Range of values for the systematic uncertainties on the signal efficiency and acceptance for each analysis bin. Uncertainties due to a particular source are treated as fully correlated between bins, while uncertainties due to different sources are treated as uncorrelated.

Source	Fractional uncertainty [%]		
	TChiHH(225,1)	TChiHH(400,1)	TChiHH(700,1)
Trigger efficiency	1–6	1–6	1–6
b tagging efficiency	1–6	1–5	2–5
Fast sim. b tagging efficiency	3–11	3–8	3–12
Fast sim. of $p_{\mathrm{T}}^{\mathrm{miss}}$ spectrum	14–72	1–7	1–5
Jet energy corrections	8–42	2–18	2–10
Jet energy resolution	2–45	1–14	1–8
Initial state radiation	1–4	1	1
Jet ID	1	1	1
Pileup	1–21	1–4	1–9
Integrated luminosity	3	3	3

The absence of excess event yields in data is interpreted in the context of the Higgsino simplified model discussed in Section 1. Table 3 shows typical values for the systematic uncertainties associated with the expected signal yields for three models with different Higgsino masses. The largest uncertainties arise from the jet energy corrections, jet energy resolution, pileup, and the modeling of the $p_{\mathrm{T}}^{\mathrm{miss}}$ spectrum by the fast simulation. These uncertainties can be as large as 70% for low Higgsino masses, models for which the $p_{\mathrm{T}}^{\mathrm{miss}} > 150$ GeV baseline requirement has low acceptance, but their impact is reduced for larger values of the Higgsino mass. Uncertainties associated with the modeling of the b tagging range from 1% to 12%. The uncertainties on the trigger efficiency, described in Section 5, range from 6% in the lowest $p_{\mathrm{T}}^{\mathrm{miss}}$ bin to less than 1% for $p_{\mathrm{T}}^{\mathrm{miss}} > 300$ GeV. Uncertainties due the modeling of ISR, the efficiency of the jet identification filter, and the total integrated luminosity are 1–4%.

A 95% confidence level (CL) upper limit on the production cross section of the GMSB higgsino NLSP scenario is estimated using the modified frequentist $\mathrm{CL_S}$ method [64–66], with a one-sided profile likelihood ratio test statistic in its asymptotic approximation [67]. Figure 9 shows the expected and observed exclusion limits for 35.9 fb^{-1}. The theoretical cross section at NLO+NLL [36, 37] as a function of Higgsino mass is shown as a dotted line. The upper limit on the cross section at a 95% confidence level is obtained from the global fit method, which takes into account the expected signal contribution in all of the bins. This cross section is below the theoretical cross section for Higgsino masses between roughly 225 GeV and 770 GeV, excluding this mass range.

9 Summary

We have performed a search for an excess of events in proton-proton collisions in the channel with two Higgs bosons and large missing transverse momentum, with each of the Higgs bosons reconstructed in its $\mathrm{h} \to \mathrm{b\bar{b}}$ decay. The data sample corresponds to an integrated luminosity of 35.9 fb^{-1} at $\sqrt{s} = 13$ TeV. Because the signal is rich in b quarks, while the background is dominated by $\mathrm{t\bar{t}}$ events, the analysis is binned in the number of b-tagged quarks. In each event, the mass difference between the two Higgs-boson candidates is required to be small, and the average mass of the two candidates is used in conjunction with the number of observed b tags to define signal and sideband regions. The observed event yields in these regions are used to ob-

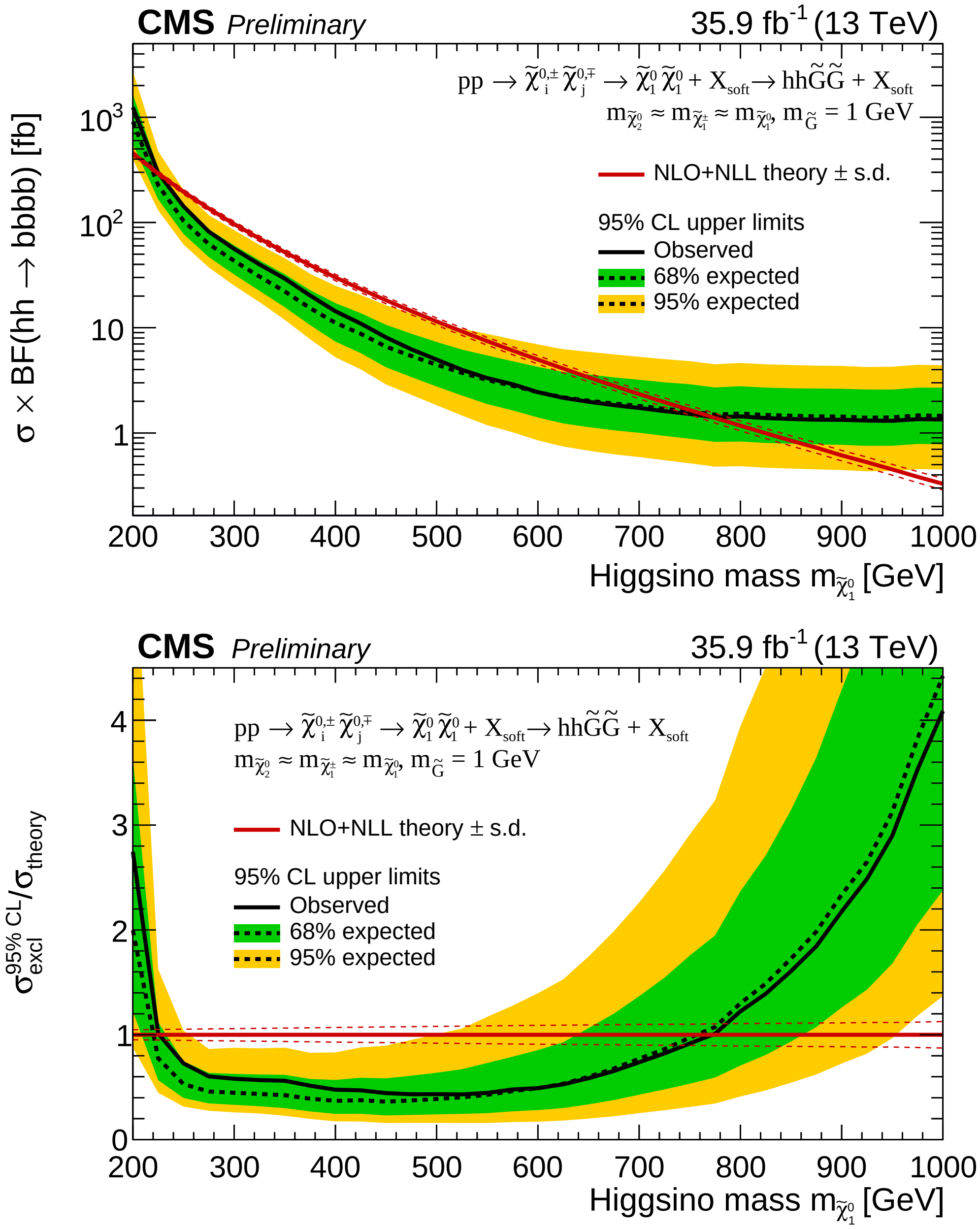

Figure 9: Top: excluded cross section times the hh→ $b\bar{b}b\bar{b}$ branching fraction at 95% CL as a function of the Higgsino mass. The theoretical cross section is shown as a dotted line. Bottom: excluded cross section at 95% CL divided by the theoretical cross section as a function of the Higgsino mass.

tain estimates for the SM background in the signal regions without input from simulated event samples. The data are also binned in regions of $|\vec{p}_{\mathrm{T}}^{\mathrm{miss}}|$ to enhance the sensitivity to the signal. The observed event yields in the signal regions are consistent with the background predictions, leading to an excluded range of Higgsino masses extending from 225 GeV to 770 GeV at 95% CL. The model used in the interpretation assumes that each Higgsino decays into a Higgs boson plus a nearly massless lightest supersymmetric particle (LSP), which is weakly interacting. Such a scenario occurs in Gauge Mediated Supersymmetry Breaking (GMSB) models, in which the LSP is a Goldstino. The cross section calculation assumes that the Higgsino sector is mass degenerate and sums over the cross sections for the pair production of all relevant combinations of Higgsinos.

References

[1] ATLAS Collaboration, "Observation of a new particle in the search for the Standard Model Higgs boson with the ATLAS detector at the LHC", *Phys. Lett. B* **716** (2012) 1, doi:10.1016/j.physletb.2012.08.020, arXiv:1207.7214.

[2] CMS Collaboration, "Observation of a new boson at a mass of 125 GeV with the CMS experiment at the LHC", *Phys. Lett. B* **716** (2012) 30, doi:10.1016/j.physletb.2012.08.021, arXiv:1207.7235.

[3] CMS Collaboration, "Observation of a new boson with mass near 125 GeV in pp collisions at $\sqrt{s}$ = 7 and 8 TeV", *JHEP* **06** (2013) 081, doi:10.1007/JHEP06(2013)081, arXiv:1303.4571.

[4] CMS Collaboration, "Precise determination of the mass of the Higgs boson and tests of compatibility of its couplings with the standard model predictions using proton collisions at 7 and 8 TeV", *Eur. Phys. J. C* **75** (2015) 212, doi:10.1140/epjc/s10052-015-3351-7, arXiv:1412.8662.

[5] ATLAS Collaboration, "Measurement of the Higgs boson mass from the $\mathrm{H} \to \gamma\gamma$ and $\mathrm{H} \to \mathrm{ZZ}^* \to 4\ell$ channels with the ATLAS detector using 25 fb^{-1} of pp collision data", *Phys. Rev. D* **90** (2014) 052004, doi:10.1103/PhysRevD.90.052004, arXiv:1406.3827.

[6] ATLAS and CMS Collaborations, "Combined Measurement of the Higgs Boson Mass in pp Collisions at $\sqrt{s} = 7$ and 8 TeV with the ATLAS and CMS Experiments", *Phys. Rev. Lett.* **114** (2015) 191803, doi:10.1103/PhysRevLett.114.191803, arXiv:1503.07589.

[7] P. Ramond, "Dual theory for free fermions", *Phys. Rev. D* **3** (1971) 2415, doi:10.1103/PhysRevD.3.2415.

[8] Y. A. Golfand and E. P. Likhtman, "Extension of the algebra of Poincaré group generators and violation of P invariance", *JETP Lett.* **13** (1971) 323.

[9] A. Neveu and J. H. Schwarz, "Factorizable dual model of pions", *Nucl. Phys. B* **31** (1971) 86, doi:10.1016/0550-3213(71)90448-2.

[10] D. V. Volkov and V. P. Akulov, "Possible universal neutrino interaction", *JETP Lett.* **16** (1972) 438.

[11] J. Wess and B. Zumino, "A Lagrangian model invariant under supergauge transformations", *Phys. Lett. B* **49** (1974) 52, doi:10.1016/0370-2693(74)90578-4.

[12] J. Wess and B. Zumino, "Supergauge transformations in four dimensions", *Nucl. Phys. B* **70** (1974) 39, doi:10.1016/0550-3213(74)90355-1.

[13] P. Fayet, "Supergauge invariant extension of the Higgs mechanism and a model for the electron and its neutrino", *Nucl. Phys. B* **90** (1975) 104, doi:10.1016/0550-3213(75)90636-7.

[14] H. P. Nilles, "Supersymmetry, supergravity and particle physics", *Phys. Rep.* **110** (1984) 1, doi:10.1016/0370-1573(84)90008-5.

[15] CMS Collaboration, "Searches for electroweak neutralino and chargino production in channels with Higgs, Z, and W bosons in pp collisions at 8 TeV", *Phys. Rev.* **D90** (2014), no. 9, 092007, doi:10.1103/PhysRevD.90.092007, arXiv:1409.3168.

[16] CMS Collaboration, "Search for top-squark pairs decaying into Higgs or Z bosons in pp collisions at $\sqrt{s}$=8 TeV", *Phys. Lett.* **B736** (2014) 371–397, doi:10.1016/j.physletb.2014.07.053, arXiv:1405.3886.

[17] CMS Collaboration, "Search for top squark and higgsino production using diphoton Higgs boson decays", *Phys. Rev. Lett.* **112** (2014) 161802, doi:10.1103/PhysRevLett.112.161802, arXiv:1312.3310.

[18] ATLAS Collaboration, "Search for supersymmetry in events with photons, bottom quarks, and missing transverse momentum in proton-proton collisions at a centre-of-mass energy of 7 TeV with the ATLAS detector", *Phys. Lett.* **B719** (2013) 261–279, doi:10.1016/j.physletb.2013.01.041, arXiv:1211.1167.

[19] ATLAS Collaboration, "Search for direct pair production of a chargino and a neutralino decaying to the 125 GeV Higgs boson in $\sqrt{s} = 8$ TeV pp collisions with the ATLAS detector", *Eur. Phys. J. C* **75** (2015), no. 5, 208, doi:10.1140/epjc/s10052-015-3408-7, arXiv:1501.07110.

[20] CMS Collaboration, "Searches for electroweak production of charginos, neutralinos, and sleptons decaying to leptons and W, Z, and Higgs bosons in pp collisions at 8 TeV", *Eur. Phys. J.* **C74** (2014), no. 9, 3036, doi:10.1140/epjc/s10052-014-3036-7, arXiv:1405.7570.

[21] G. 't Hooft, "Naturalness, chiral symmetry, and spontaneous chiral symmetry breaking", *NATO Sci. Ser. B* **59** (1980) 135.

[22] E. Witten, "Dynamical Breaking of Supersymmetry", *Nucl. Phys. B* **188** (1981) 513, doi:10.1016/0550-3213(81)90006-7.

[23] M. Dine, W. Fischler, and M. Srednicki, "Supersymmetric Technicolor", *Nucl. Phys. B* **189** (1981) 575, doi:10.1016/0550-3213(81)90582-4.

[24] S. Dimopoulos and S. Raby, "Supercolor", *Nucl. Phys. B* **192** (1981) 353, doi:10.1016/0550-3213(81)90430-2.

[25] S. Dimopoulos and H. Georgi, "Softly Broken Supersymmetry and SU(5)", *Nucl. Phys. B* **193** (1981) 150, doi:10.1016/0550-3213(81)90522-8.

[26] R. K. Kaul and P. Majumdar, "Cancellation of Quadratically Divergent Mass Corrections in Globally Supersymmetric Spontaneously Broken Gauge Theories", *Nucl. Phys. B* **199** (1982) 36, doi:10.1016/0550-3213(82)90565-X.

[27] S. Dimopoulos and G. F. Giudice, "Naturalness constraints in supersymmetric theories with nonuniversal soft terms", *Phys. Lett. B* **357** (1995) 573, doi:10.1016/0370-2693(95)00961-J, arXiv:hep-ph/9507282.

[28] R. Barbieri and D. Pappadopulo, "S-particles at their naturalness limits", *JHEP* **10** (2009) 061, doi:10.1088/1126-6708/2009/10/061, arXiv:0906.4546.

[29] M. Papucci, J. T. Ruderman, and A. Weiler, "Natural SUSY endures", *JHEP* **09** (2012) 035, doi:10.1007/JHEP09(2012)035, arXiv:1110.6926.

[30] J. L. Feng, "Naturalness and the Status of Supersymmetry", *Ann. Rev. Nucl. Part. Sci.* **63** (2013) 351, doi:10.1146/annurev-nucl-102010-130447, arXiv:1302.6587.

[31] G. R. Farrar and P. Fayet, "Phenomenology of the Production, Decay, and Detection of New Hadronic States Associated with Supersymmetry", *Phys. Lett. B* **76** (1978) 575, doi:10.1016/0370-2693(78)90858-4.

[32] ATLAS Collaboration, "Search for new phenomena in final states with an energetic jet and large missing transverse momentum in pp collisions at $\sqrt{s}$ =8 TeV with the ATLAS detector", *Eur. Phys. J.* **C75** (2015), no. 7, 299, doi:10.1140/epjc/s10052-015-3517-3, 10.1140/epjc/s10052-015-3639-7, arXiv:1502.01518. [Erratum: Eur. Phys. J.C75,no.9,408(2015)].

[33] CMS Collaboration, "Search for dark matter, extra dimensions, and unparticles in monojet events in proton-proton collisions at $\sqrt{s} = 8$ TeV", *Eur. Phys. J. C* **75** (2015), no. 5, 235, doi:10.1140/epjc/s10052-015-3451-4, arXiv:1408.3583.

[34] S. Dimopoulos, M. Dine, S. Raby, and S. D. Thomas, "Experimental signatures of low-energy gauge mediated supersymmetry breaking", *Phys. Rev. Lett.* **76** (1996) 3494–3497, doi:10.1103/PhysRevLett.76.3494, arXiv:hep-ph/9601367.

[35] K. T. Matchev and S. D. Thomas, "Higgs and Z boson signatures of supersymmetry", *Phys. Rev.* **D62** (2000) 077702, doi:10.1103/PhysRevD.62.077702, arXiv:hep-ph/9908482.

[36] B. Fuks, M. Klasen, D. R. Lamprea, and M. Rothering, "Gaugino production in proton-proton collisions at a center-of-mass energy of 8 TeV", *JHEP* **10** (2012) 081, doi:10.1007/JHEP10(2012)081, arXiv:1207.2159.

[37] B. Fuks, M. Klasen, D. R. Lamprea, and M. Rothering, "Precision predictions for electroweak superpartner production at hadron colliders with RESUMMINO", *Eur. Phys. J. C* **73** (2013) 2480, doi:10.1140/epjc/s10052-013-2480-0, arXiv:1304.0790.

[38] J. Alwall, P. Schuster, and N. Toro, "Simplified models for a first characterization of new physics at the LHC", *Phys. Rev. D* **79** (2009) 075020, doi:10.1103/PhysRevD.79.075020, arXiv:0810.3921.

[39] J. Alwall, M.-P. Le, M. Lisanti, and J. G. Wacker, "Model-independent jets plus missing energy searches", *Phys. Rev. D* **79** (2009) 015005, doi:10.1103/PhysRevD.79.015005, arXiv:0809.3264.

[40] D. Alves et al., "Simplified models for LHC new physics searches", *J. Phys. G* **39** (2012) 105005, doi:10.1088/0954-3899/39/10/105005, arXiv:1105.2838.

[41] CMS Collaboration, "The CMS experiment at the CERN LHC", *JINST* **3** (2008) S08004, doi:10.1088/1748-0221/3/08/S08004.

[42] J. Alwall et al., "The automated computation of tree-level and next-to-leading order differential cross sections, and their matching to parton shower simulations", *JHEP* **07** (2014) 079, doi:10.1007/JHEP07(2014)079, arXiv:1405.0301.

[43] S. Alioli, P. Nason, C. Oleari, and E. Re, "NLO single-top production matched with shower in POWHEG: *s*- and *t*-channel contributions", *JHEP* **09** (2009) 111, doi:10.1007/JHEP02(2010)011, 10.1088/1126-6708/2009/09/111, arXiv:0907.4076. [Erratum: *JHEP* **02** (2010) 011].

[44] E. Re, "Single-top Wt-channel production matched with parton showers using the POWHEG method", *Eur. Phys. J. C* **71** (2011) 1547, doi:10.1140/epjc/s10052-011-1547-z, arXiv:1009.2450.

[45] NNPDF Collaboration, "Parton distributions for the LHC Run II", *JHEP* **04** (2015) 040, doi:10.1007/JHEP04(2015)040, arXiv:1410.8849.

[46] T. Sjöstrand et al., "An Introduction to PYTHIA 8.2", *Comput. Phys. Commun.* **191** (2015) 159, doi:10.1016/j.cpc.2015.01.024, arXiv:1410.3012.

[47] CMS Collaboration, "Event generator tunes obtained from underlying event and multiparton scattering measurements", *Eur. Phys. J. C* **76** (2016), no. 3, 155, doi:10.1140/epjc/s10052-016-3988-x, arXiv:1512.00815.

[48] GEANT4 Collaboration, "GEANT4 — a simulation toolkit", *Nucl. Instrum. Meth. A* **506** (2003) 250, doi:10.1016/S0168-9002(03)01368-8.

[49] CMS Collaboration, "The fast simulation of the CMS detector at LHC", *J. Phys. Conf. Ser.* **331** (2011) 032049, doi:10.1088/1742-6596/331/3/032049.

[50] CMS Collaboration, "Particle flow event reconstruction in CMS and performance for jets, taus and $E_{\mathrm{T}}^{\mathrm{miss}}$", CMS Physics Analysis Summary CMS-PAS-PFT-09-001, CERN, 2009.

[51] CMS Collaboration, "Commissioning of the particle-flow event reconstruction with the first LHC collisions recorded in the CMS detector", CMS Physics Analysis Summary CMS-PAS-PFT-10-001, CERN, 2010.

[52] M. Cacciari, G. P. Salam, and G. Soyez, "The anti-k_{t} jet clustering algorithm", *JHEP* **04** (2008) 063, doi:10.1088/1126-6708/2008/04/063, arXiv:0802.1189.

[53] M. Cacciari, G. P. Salam, and G. Soyez, "FastJet User Manual", *Eur. Phys. J.* **C72** (2012) 1896, doi:10.1140/epjc/s10052-012-1896-2, arXiv:1111.6097.

[54] M. Cacciari and G. P. Salam, "Pileup subtraction using jet areas", *Phys. Lett. B* **659** (2008) 119, doi:10.1016/j.physletb.2007.09.077, arXiv:0707.1378.

[55] CMS Collaboration, "Determination of jet energy calibration and transverse momentum resolution in CMS", *JINST* **6** (2011) P11002, doi:10.1088/1748-0221/6/11/P11002, arXiv:1107.4277.

[56] CMS Collaboration, "Heavy flavor identification at CMS with deep neural networks", CMS Detector Performance Report CMS-DP-2017-005, CERN, 2017.

[57] D. Guest et al., "Jet Flavor Classification in High-Energy Physics with Deep Neural Networks", *Phys. Rev. D* **94** (2016), no. 11, 112002, doi:10.1103/PhysRevD.94.112002, arXiv:1607.08633.

[58] CMS Collaboration, "Identification of b-quark jets with the CMS experiment", *JINST* **8** (2013) P04013, doi:10.1088/1748-0221/8/04/P04013, arXiv:1211.4462.

[59] CMS Collaboration, "Identification of b quark jets at the CMS Experiment in the LHC Run 2", CMS Physics Analysis Summary CMS-PAS-BTV-15-001, CERN, 2016.

[60] CMS Collaboration, "Performance of electron reconstruction and selection with the CMS detector in proton-proton collisions at $\sqrt{s} = 8$ TeV", *JINST* **10** (2015) P06005, doi:10.1088/1748-0221/10/06/P06005, arXiv:1502.02701.

[61] CMS Collaboration, "Performance of CMS muon reconstruction in pp collision events at $\sqrt{s} = 7$ TeV", *JINST* **7** (2012) P10002, doi:10.1088/1748-0221/7/10/P10002, arXiv:1206.4071.

[62] K. Rehermann and B. Tweedie, "Efficient Identification of Boosted Semileptonic Top Quarks at the LHC", *JHEP* **03** (2011) 059, doi:10.1007/JHEP03(2011)059, arXiv:1007.2221.

[63] CMS Collaboration, "Search for supersymmetry in pp collisions at sqrt(s) = 13 TeV in the single-lepton final state using the sum of masses of large-radius jets", arXiv:1605.04608.

[64] T. Junk, "Confidence level computation for combining searches with small statistics", *Nucl. Instrum. Meth. A* **434** (1999) 435, doi:10.1016/S0168-9002(99)00498-2, arXiv:hep-ex/9902006.

[65] A. L. Read, "Presentation of search results: The CL_S technique", *J. Phys. G* **28** (2002) 2693, doi:10.1088/0954-3899/28/10/313.

[66] ATLAS Collaboration, CMS Collaboration, LHC Higgs Combination Group, "Procedure for the LHC Higgs boson search combination in Summer 2011", Technical Report CMS-NOTE-2011-005, ATL-PHYS-PUB-2011-11, CERN, 2011.

[67] G. Cowan, K. Cranmer, E. Gross, and O. Vitells, "Asymptotic formulae for likelihood-based tests of new physics", *Eur. Phys. J. C* **71** (2011) 1554, doi:10.1140/epjc/s10052-011-1554-0, arXiv:1007.1727. [Erratum: doi:10.1140/epjc/s10052-013-2501-z].